Bio-Design and Manufacturing (2024) 7:651–669
https://doi.org/10.1007/s42242-024-00280-8

RESEARCH ARTICLE

In vitro investigations on the effects of graphene and graphene oxide on polycaprolactone bone tissue engineering scaffolds

Yanhao Hou[1] · Weiguang Wang[1] · Paulo Bartolo[1,2]

Received: 3 July 2023 / Accepted: 27 March 2024 / Published online: 2 August 2024

Abstract

Polycaprolactone (PCL) scaffolds that are produced through additive manufacturing are one of the most researched bone tissue engineering structures in the field. Due to the intrinsic limitations of PCL, carbon nanomaterials are often investigated to reinforce the PCL scaffolds. Despite several studies that have been conducted on carbon nanomaterials, such as graphene (G) and graphene oxide (GO), certain challenges remain in terms of the precise design of the biological and nonbiological properties of the scaffolds. This paper addresses this limitation by investigating both the nonbiological (element composition, surface, degradation, and thermal and mechanical properties) and biological characteristics of carbon nanomaterial-reinforced PCL scaffolds for bone tissue engineering applications. Results showed that the incorporation of G and GO increased surface properties (reduced modulus and wettability), material crystallinity, crystallization temperature, and degradation rate. However, the variations in compressive modulus, strength, surface hardness, and cell metabolic activity strongly depended on the type of reinforcement. Finally, a series of phenomenological models were developed based on experimental results to describe the variations of scaffold's weight, fiber diameter, porosity, and mechanical properties as functions of degradation time and carbon nanomaterial concentrations. The results presented in this paper enable the design of three-dimensional (3D) bone scaffolds with tuned properties by adjusting the type and concentration of different functional fillers.

Graphic abstract

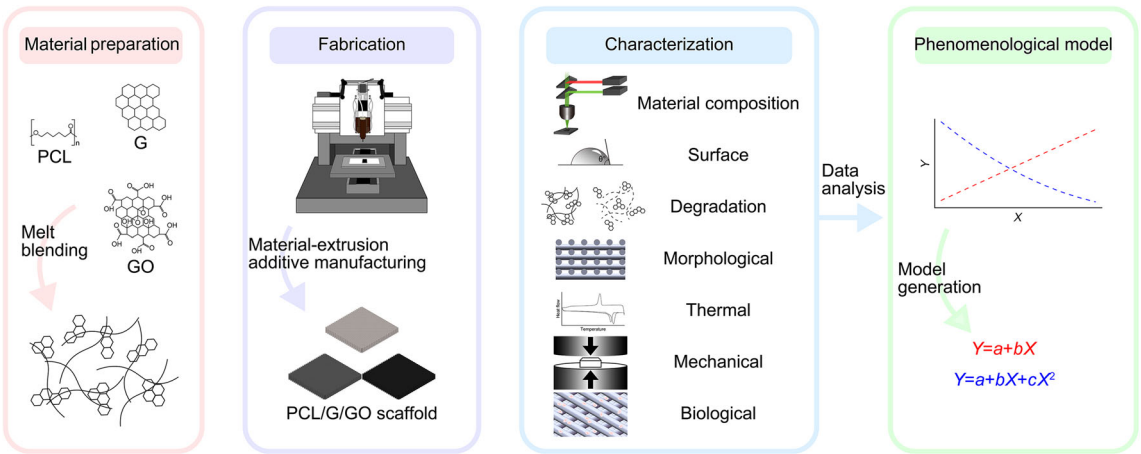

Keywords Additive manufacturing · Bone tissue engineering · Carbon nanomaterial · Graphene · Graphene oxide · Scaffold

✉ Weiguang Wang
weiguang.wang@manchester.ac.uk

✉ Paulo Bartolo
paulojorge.dasilvabartolo@manchester.ac.uk;
pbartolo@ntu.edu.sg

Introduction

Advanced manufacturing technologies and novel materials have facilitated the development of new scaffold-based strategies in tissue engineering. The main design requirements of bone tissue engineering scaffolds are related to their mechanical properties (ability to withstand physiological loads), surface properties (ability to bond with the surrounding tissues, allowing cell ingrowth), degradability (degradation rate must match bone regeneration and must degrade into nontoxic products), and biocompatibility [1–3].

Material extrusion additive manufacturing presents unique advantages in the fabrication of biocompatible and biodegradable polymeric bone tissue engineering scaffolds. Using a layer-by-layer fabrication approach, this process can selectively deposit a wide range of materials, with high customization, high accuracy, high repeatability, and relatively low fabrication costs [4–8]. Besides, different polymeric or ceramic materials have been considered for bone scaffold fabrication [9]. However, the use of these materials alone presents several limitations, making it difficult for scaffolds to meet the design requirements. Ceramic materials exhibit limited biomechanical properties due to intrinsic brittleness, difficulty in controlling degradation and resorption rates, being also difficult to process [10–12], whereas commonly used polymers tend to cause inflammatory effects due to acid degradation products, the lack of cell recognition sites, and limited mechanical properties and bioactivity [13–15]. Therefore, a variety of functional fillers, particularly carbon nanomaterials, such as graphene (G), graphene oxide (GO), reduced graphene oxide (rGO), and carbon nanotubes (CNTs), have been investigated to enhance various properties, such as mechanical properties, electrical conductivity, degradability, and biological behaviors [16–18].

Among these carbon nanomaterials, the unique significance of two-dimensional (2D) carbon nanomaterials, G and GO, lies in their ability to simultaneously enhance various critical scaffold properties, such as electrical conductivity, degradability, and surface, thermal, mechanical, and biological properties. With superior electrical conductivity, G presents a promising trend in engineering electrically active tissue engineering scaffolds [19]. It has been reported that electrical conductivity improved from 6.13×10^{-8} S/m to 13 S/m by adding 5% (volume fraction) of G into bioglass [20]. Promoted in vivo new bone regeneration was also observed by using three-dimensional (3D)-printed electroactive bone scaffolds containing G as the functional filler [21]. In order to modify the electrical conductivity of tissue engineering scaffolds, GO, which exhibits electrical conductivity significantly lower than G (primarily dependent on the oxidation degree of GO) [22], has also been widely used. By adding GO, the electrical conductivity can be improved from 1.63×10^{-3} S/m to 0.134 S/m, hence enhancing cell viability [23]. Moreover, G has been reported to improve the mechanical properties of scaffolds, such as Young's modulus, compressive strength, fracture toughness, and hardness [24, 25]. G can also increase piezoelectric efficacy, hydrophilicity, and protein adsorption, contributing to better biological performance [26, 27]. Moreover, several in vitro studies have shown that the addition of G improves cell adhesion, proliferation, and differentiation [26–28]. Scaffolds containing G were also successfully used to deliver antibiotics and anticancer drugs for eradicating *Escherichia coli* and *Staphylococcus aureus* in vitro [29]. Promising in vivo results on ablating MG-63 osteosarcoma cancer cells and promoting new bone regeneration have also been reported [29]. Similarly, several other studies have shown improved crystallization, mechanical properties (e.g., the load to failure, stiffness, and tensile and compressive modulus and strength), piezoelectric performance, hydrophilicity, and degradability (attributed to the abundant hydrophilic functional groups) upon the addition of GO to polyvinylidene fluoride, poly-L-lactic acid, and platelet-rich plasma gels [30–32]. Additionally, the addition of GO increases protein adsorption, promoting cell adhesion, viability, differentiation, and mineralization, by upregulating osteogenic-related gene expression [31–33]. Similar results were observed through in vivo studies using mouse and rabbit models [32, 34]. Other carbon nanomaterials such as rGO and CNTs have also been investigated as functional fillers. rGO has been reported to enhance the elastic modulus, compressive strength, ductility, wettability, and the degradation rate of scaffolds due to the presence of oxygen-containing functional groups, grain refinement, and micro-galvanic effects [35–37]. Enhanced cell adhesion, proliferation, osteogenic differentiation, and faster bone repair were observed both in vitro [37] and in vivo [38, 39]. The addition of CNTs increases mechanical properties due to bridging mechanisms and increased crystallinity, accelerating the scaffold's degradation kinetics, increasing hydrophilicity, and enhancing scaffold's biological performance [40–43].

However, the abovementioned studies are limited, and the effects of adding these carbon nanomaterials and their concentrations are not systematically compared. Moreover, scaffolds are designed according to predefined properties to be achieved once printed, but these properties are significantly affected by the degradation process, which may compromise their long-term performance. Thus, it is crucial to understand the impacts of these fillers on the degradation kinetics and their corresponding effects on other relevant

[1] School of Engineering, Faculty of Science and Engineering, The University of Manchester, Manchester, UK

[2] Singapore Centre for 3D Printing, School of Mechanical and Aerospace Engineering, Nanyang Technological University, Singapore, Singapore

properties. Furthermore, the development of phenomenological models that describe the effects of different fillers and their concentrations is of extreme importance in designing more suitable scaffolds with tuned properties, considering their long-term behaviors. This can reduce the research cost and accelerate the development process.

In this research, two types of carbon nanomaterials, G and GO, were considered as functional fillers, and incorporated into polycaprolactone (PCL) scaffolds at different concentrations (1%, 3%, 5%, and 7%, mass fraction). Although these are highly relevant fillers for bone tissue engineering applications, limited information has been presented in comparing both fillers. Therefore, in-depth investigations were conducted to study and compare the impacts of these carbon nanomaterials on 3D-printed PCL scaffolds, especially in terms of surface properties, element composition, degradation kinetics, crystallinity, and mechanical and biological properties. Phenomenological models that can be used to design scaffolds with ideal properties were also generated based on the experimental results.

Materials and methods

Scaffold design and fabrication

PCL pellets Capa 6500 (Perstorp, UK) and GO nanosheets (Sigma-Aldrich, UK) were used as received from the suppliers. G nanosheets were synthesized through water-assisted liquid-phase exfoliation of graphite, as previously reported [26]. Briefly, *N*-methyl-2-pyrotanone (99% extra pure, Acros Organics, USA) containing 20% (mass fraction) of water was used to impregnate 50 mg of microcrystalline graphite powder (325 mesh, 99.995% pure, Alfa Aesar, UK). The materials were sonicated and hung overnight, followed by centrifugation. The upper 75% (volume fraction) of the colloidal supernatant was collected and dried to obtain the G nanosheets. Next, the PCL/G and PCL/GO composite materials were prepared through a melt blending method at desired concentrations (1%, 3%, 5%, and 7%, mass fraction, corresponding to G1, G3, G5, G7, GO1, GO3, GO5, and GO7) as previously reported [44, 45]. The designed scaffolds with a fiber diameter of 330 μm, pore size of 350 μm from the top view, pore size of 210 μm from the side view, and 0°/90° lay-down pattern were fabricated using a pellet-based screw-assisted material-extrusion 3D printing system 3D Discovery (regenHU, Switzerland) at room temperature (controlled at 22 °C by air conditioning) following previously reported optimized processing parameters [44, 45]. The cost of each fabricated scaffold is approximately $3, including energy and material costs, which is significantly lower than that of commercial products. All scaffolds were produced in the size of 32.0 mm × 32.0 mm × 3.2 mm and cut into the desired dimensions for different characterization tests.

Material composition

Fourier-transform infrared spectroscopy (FTIR) analysis

FTIR analysis was conducted to confirm the presence of functional groups on the obtained G and received GO. A Vertex 70 FTIR spectrometer (Bruker, USA) was used, and the tests were run in a range of 400 to 4000 cm^{-1} in transmittance mode.

Raman spectroscopy analysis

Raman spectroscopy analysis was carried out to verify the presence of G and GO in the scaffolds using a Renishaw inVia confocal Raman microscope (Renishaw, UK) with a laser (432 nm) at an intensity of 10 and the exposure of 10 s, with a grating of 1200 g/mm in regular mode and under 50× magnification.

Energy dispersive X-ray spectroscopy (EDX) analysis

The element composition of the scaffolds, particularly the concentrations of carbon (C) and oxygen (O), was analyzed through EDX on a TESCAN MIRA3 system (TESCAN, Czech). The scaffolds were cut into the size of 4.0 mm × 4.0 mm × 3.2 mm and coated with gold–palladium (4:1, mass ratio, 6 nm thick) using a Q150T ES sputter coater (Quorum Technologies, UK). The element composition was analyzed using the Oxford AZtec software (Oxford Instruments, UK) based on the acquired images.

Surface properties

Laser scanning confocal analysis

The surface roughness of the scaffolds was evaluated by laser scanning confocal microscopy using a KEYENCE VK-X200K shape measurement laser microscope (Keyence, Japan). The images of the scaffolds' top surface were captured under laser mode at 150× magnification. The Gwyddion software (Czech Metrology Institute, Czech) was used for surface profile analysis and surface roughness calculation.

Nanoindentation analysis

The surface hardness and reduced modulus of the scaffolds were determined by conducting nanoindentation tests on a HYSITRON TI 950 TriboIndentor (Bruker, USA), which was equipped with a Berkovich tip (three-sided pyramidal). The

nanoindentation tests were conducted using a 5 mN load cell (given approximately 2 μm depth) with a load profile of 5 s load at a rate of 0.8 μN/s, 2 s hold at peak load (P_{max}), and 5 s unload at a rate of 0.8 μN/s. The force and displacement were recorded during the test, and the hardness (H) was calculated based on P_{max} and contact area (A) according to the following equation:

$$H = \frac{P_{max}}{A}. \quad (1)$$

The reduced modulus (E) was calculated using the Oliver–Pharr model, using the contact stiffness (S) and A as follows:

$$E = \frac{S \times \sqrt{\pi}}{2 \times \sqrt{A}}. \quad (2)$$

Water contact angle analysis

The scaffold's surface wettability was assessed by measuring the water contact angle using a DSA100E drop shape analyzer (Krüss, Germany). Briefly, 1 mL of deionized water was dropped on the scaffold, and the droplet profiles were recorded at 0 s and 15 s. These were then analyzed using the Drop Shape Analysis software (Krüss, Germany) according to the sessile drop technique.

In vitro degradation characterization

Due to the long-term degradation of PCL under physiological conditions, accelerated degradation studies were conducted until the scaffolds lost their structural stability, as this is a useful tool to rapidly provide data on how different materials behave. Moreover, PCL in vitro and in vivo degrades in the initial stages, at high molecular weights, through hydrolytic random scission [46, 47]. By using an alkali such as sodium hydroxide, hydrolysis is accelerated due to the high concentration of OH^-. Thus, accelerated degradation maintains a hydrolytic degradation pathway, providing relevant information to understand the in vivo degradation kinetics of the scaffolds.

In this case, the scaffolds were cut to approximately 0.5 g weight, after which they were rinsed and air-dried overnight. The initial mass of each scaffold was measured before degradation (D0). The scaffolds were placed in glass vials, added with 2 mL of 5 mol/L sodium hydroxide solution, and incubated under standard conditions (37 °C, 95% humidity, and 5% CO_2). At each time point, the scaffolds were washed, air-dried, and weighed again. The mass change is presented as the percentage of the initial weight before degradation, as follows:

$$\text{Mass}(t) = \frac{M(t)}{M_0} \times 100\%, \quad (3)$$

where $M(t)$ represents the scaffold weight after degradation time t (expressed in hours) and M_0 represents the original scaffold weight. The pH value was maintained at approximately 13.5 during the degradation characterization.

Morphological characterization

The morphology of the scaffolds before and during degradation was characterized through scanning electron microscopy (SEM) imaging, using a TESCAN MIRA3 system (TESCAN, Czech). The scaffolds were cut into the size of 4.0 mm × 4.0 mm × 3.2 mm and gold–palladium coated. The top surface, cross-section, and close-up view were imaged considering an accelerating voltage of 2 kV. The captured images were analyzed using the ImageJ software (NIH, USA).

Thermal analysis

Thermogravimetric analysis

The concentrations of G and GO in the scaffolds and the scaffolds' thermal stability were determined by conducting thermogravimetric analysis using a Thermal Analysis Q500 analyzer (TA Instrument, USA). The scaffolds were cut into the weight of approximately 10 mg and placed in platinum pans. The scans were conducted in a nitrogen atmosphere with a flow rate of 90 mL/min, with the temperature ranging from 30 to 555 °C at 10 °C/min. The obtained results were analyzed using the Universal Analysis software (TA Instrument, USA).

Differential scanning calorimetry (DSC) analysis

The crystallinity (χ_c) and thermal transitions [e.g., glass transition temperature (T_g), crystallization temperature (T_c), and melting temperature (T_m)] were determined by performing differential scanning calorimetry analysis using a Q100 differential scanning calorimeter (TA Instrument, USA). The scaffolds were cut into approximately 10 mg, sealed in aluminum pans and lids, and then subjected to a nitrogen atmosphere at a flow rate of 50 mL/min. The scaffolds were first heated from −90 to 100 °C at 10 °C/min, and then cooled down from 100 to −90 °C at 10 °C /min. The temperature was maintained for 2 min, after which the scaffolds were heated up again from −90 to 100 °C at 10 °C /min. The first heating cycle represented the thermal characteristics of the scaffold after the printing process. After removing the previous thermal history, the second heating cycle presents the intrinsic thermal properties of the material. The first and second heating curves helped to determine T_g, T_m, melting enthalpy (ΔH_m), and χ_c, while the cooling curve provided T_c, crystallization enthalpy (ΔH_c), and χ_c. In particular, χ_c

is determined as follows:

$$\chi_c = \frac{\Delta H_m/\Delta H_c}{\Delta H_m^0} \times \frac{100}{w}, \quad (4)$$

where $\Delta H_m/\Delta H_c$ is the experimental melting or crystallization enthalpy, ΔH_m^0 (139.5 J/g) is the melting enthalpy of 100% crystalline PCL, and w is the weight fraction of PCL.

Mechanical characterization

Compressive modulus and compressive strength were determined through uniaxial mechanical compression tests using an INSTRON X testing system (High Wycombe, UK), according to the American Society for Testing and Materials (ASTM) standards [48, 49]. The scaffolds were cut into 3.0 mm × 3.0 mm × 3.2 mm and then compressed from the strain of 0 to 0.3 mm/mm (30%) at a compression rate of 0.5 mm/min using a 100 N load cell. The strain and stress were recorded during the test and the compressive modulus and compressive strength were analyzed using the Origin software (OriginLab, USA).

In vitro biological characterization

Human adipose-derived stem cells (hADSCs, passages 6 to 8, Invitrogen, USA) were used for in vitro cell proliferation tests, which were conducted after 1, 3, 5, and 7 d of cell seeding using the Alamar Blue assay. Before cell seeding, cells were cultured with MesenPRO RS Basal medium (Thermo Fisher Scientific, USA). After the scaffolds were sterilized, washed, and air-dried, approximately 25,000 cells were seeded on each scaffold and then incubated under standard conditions, following the supplier's instructions. At each time point, 0.5 mL of medium containing 0.001% (0.01 g/L) resazurin sodium salt (Sigma-Aldrich, UK) was added to the cell-seeded scaffolds. After incubated under standard conditions for 4 h, 150 μL of medium from each well was transferred into a 96-well plate (Corning, USA) and the fluorescence intensity was measured using a CLARIOstar microplate reader (BMG LABTECH, Germany) at an excitation wavelength of 540 nm and emission wavelength of 590 nm.

The morphology of the cells on the scaffolds was analyzed using confocal imaging. The cell-seeded scaffolds, which were previously fixed using 10% (volume fraction) formalin, were washed and 0.1% (volume fraction) Triton X-100 (Sigma-Aldrich, UK) was added. Then phosphate-buffered saline (PBS) containing 5% (volume fraction) fetal bovine serum (Sigma-Aldrich, UK) was added to the cell-seeded scaffolds and then stood for 1 h. After washing the cell-seeded scaffolds, they were stained with Alexa Fluor 488 phalloidin (Thermo Fisher Scientific, USA) and 4′,6-diamidino-2-phenylindole (DAPI; Thermo Fisher Scientific, USA) according to the manufacturer's instructions. The confocal images were obtained using a Leica SP8 LIGHTNING confocal microscope (Leica, Germany).

Data analysis

All experiments were conducted with at least three scientific repetitions ($n \geq 3$), and the results were reported as mean ± standard deviation. All results were statistically analyzed via one-way analysis of variance (ANOVA) with Tukey post hoc tests using the Origin software (OriginLab, USA). The significance levels were set at $^{*}P < 0.05$, $^{**}P < 0.01$, and $^{***}P < 0.001$ compared with PCL; $^{\#}P < 0.05$, $^{\#\#}P < 0.01$, and $^{\#\#\#}P < 0.001$ compared among the same material with different concentrations; and $^{\&}P < 0.05$, $^{\&\&}P < 0.01$, and $^{\&\&\&}P < 0.001$ compared between different materials with the same concentration. All curve-fitted results were fitted using linear and polynomial fitting.

Results and discussion

Material and scaffolds characterization

Material incorporation verification

Figure 1a shows the FTIR spectra of G and GO. The results shown in the figure indicated the presence of functional groups, particularly the C≡C (2029 and 2159 cm^{-1}) group in G, and O–H (3177 cm^{-1}), C–H (2873 cm^{-1}), C=O (1731 cm^{-1}), C=C (1621 cm^{-1}), and C–O (1279, 1139, and 1039 cm^{-1}) groups in GO. Figure 1b shows the Raman spectra of the PCL, G, and GO scaffolds at different concentrations. The results revealed two typical features of carbon nanomaterials: D and G bands. The D band was observed at approximately 1350 cm^{-1}, corresponding to scattering from local defects or disorders present in carbon [50, 51], whereas the G band was observed at approximately 1580 cm^{-1}, corresponding to the in-plane tangential stretching of the C–C bonds in the graphitic structure [50, 51]. These features indicate that G and GO were successfully incorporated into the PCL scaffolds.

Surface roughness analysis

The laser scanning confocal microscopy results showed that the addition of G and GO significantly altered the surface topography of the scaffolds. As observed from Figs. 1c and 1d, the incorporation of G and GO eliminated the deep valleys observed on the surface of the PCL scaffolds. Scaffolds containing G and GO exhibited lower arithmetic mean height (Sa) and root mean square height (Sq) than PCL scaffolds, following a similar trend previously reported for the addition

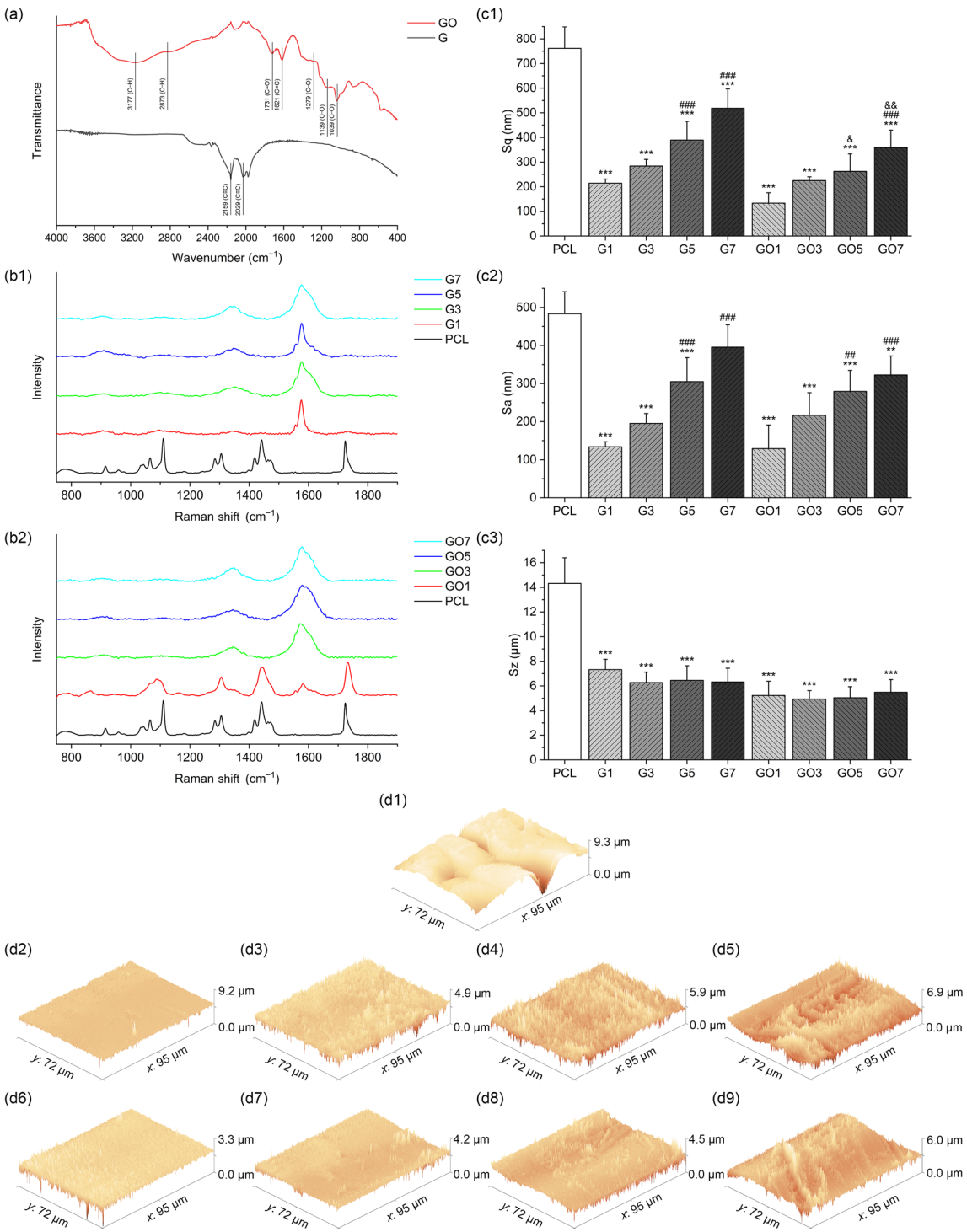

Fig. 1 **a** Fourier-transform infrared spectroscopy (FTIR) spectra of graphene (G) and graphene oxide (GO). **b** Raman spectra of polycaprolactone (PCL) scaffolds and different (**b1**) G and (**b2**) GO scaffolds. **c** Surface roughness and **d** surface profiles of PCL scaffolds and different G and GO scaffolds. **c1** Root mean square height (Sq); **c2** arithmetic mean height (Sa); **c3** maximum height (Sz). **d1** PCL; **d2–d5** G1, G3, G5, and G7; **d6–d9** GO1, GO3, GO5, and GO7. 1, 3, 5, and 7: 1%, 3%, 5%, and 7% (mass fraction). The results were reported as mean ± standard deviation, $n = 5$. $^{**}P < 0.01$ and $^{***}P < 0.001$: compared with PCL; $^{\#\#}P < 0.01$ and $^{\#\#\#}P < 0.001$: compared among the same material with different concentrations; $^{\&}P < 0.05$ and $^{\&\&}P < 0.01$: compared between different materials with the same concentration

of GO into poly(vinylidene fluoride) membranes [52]. However, this observation differed from other reported studies that used linear measurements (Ra and Rq) [53, 54]. Compared with areal measurements (Sa and Sq), the use of linear measurements may result in the loss of the valley profile. Thus, Sa and Sq seem to be more suitable for the description of surface roughness. Furthermore, the increase in Sa and Sq was proportional to G and GO concentrations, which can be attributed to changes in the material's rheological properties (viscosity, viscoelastic properties, and shear-thinning). These changes made G and GO more difficult to align during the material preparation and scaffold fabrication process. Similar results were observed when incorporating GO [54, 55], rGO [56], and CNTs [41] into PCL scaffolds. However, all G and GO scaffolds exhibited similar maximum heights (Sz) that were significantly lower than that of PCL scaffolds.

Surface mechanical properties analysis

Figure 2a presents the surface hardness and surface reduced modulus of the scaffolds before degradation. The results showed that the addition of G only had minor effects on the hardness of the scaffolds, whereas the addition of GO exhibited considerably enhanced effects. The hardness increased by increasing G and GO concentrations, with the highest value of (0.0513 ± 0.0015) GPa (GO7). However, this value is still lower than the hardness of wet adult human bone (approximately 0.5 GPa) [57, 58]. Regarding the reduced modulus, both G and GO exhibited significant enhancement effects, with the reduced modulus increasing by increasing the G and GO concentrations, clearly indicating the reinforcement effects of G and GO on the PCL matrix.

Surface wettability analysis

As shown in Figs. 2b–2d, the water contact angle decreased with the addition of G and GO. Scaffolds with higher G and GO concentrations presented lower water contact angles, corresponding to typical hydrophobic surfaces [59, 60]. The results also showed that the incorporation of GO had a slightly higher impact on the water contact angle than G, but no statistical differences were observed. The change in the water contact angle can be attributed to the surface roughness change caused by the addition of carbon nanomaterials [52], as well as oxygen-containing hydrophilic groups (e.g., O, OH, and COOH) [61, 62], which have a negative charge, forming hydrogen bonds, leading to the increase in hydrophilicity [63, 64]. Moreover, the results revealed that the water contact angle slightly decreased after 15 s, indicating that the water was absorbed by the scaffolds.

In vitro degradation

Variations in scaffold element compositions with time

The EDX results are presented in Fig. 3a, showing that the weight ratio of carbon (C) on the scaffolds slightly increased by increasing G and GO concentrations. Moreover, compared with the scaffolds before degradation, the weight ratios of C on all G and GO scaffolds slightly increased right after starting the degradation process. These slight increases can be attributed to the released G and GO reattached on the fiber surface, which was not completely washed from the scaffolds during scaffold collection. However, the weight ratio of C remained relatively stable throughout the degradation time, indicating that the degradation process did not affect the composition of the scaffolds.

Variations in filler concentrations with time

Thermogravimetric results showed that both G and GO were effectively incorporated into the scaffolds at designed concentrations (Fig. 3b), without significant mass loss or decomposition during both material preparation and scaffold fabrication. Moreover, it was possible to observe a minor increase in the filler weight ratio throughout degradation, but without significant statistical differences. This minor increase confirms the EDX results and can be attributed to the G and GO left on the scaffolds. Moreover, no significant filler concentration change was observed during the degradation of all scaffolds, indicating that both G and GO were released into the medium, with a relatively constant release rate throughout the degradation process.

Variations in thermal properties with time

The DSC results showed that the addition of G and GO significantly increased χ_c of the PCL scaffolds (Fig. 3c). It is also possible to observe that χ_c increases by increasing both G and GO concentrations, but statistically significant differences can only be observed at relatively high concentrations (G5, G7, GO5, and GO7). The increase in χ_c can be attributed to the nucleating actions of G and GO in the PCL matrix [65, 66]. Previous studies have shown that the incorporation of G increases the number of crystallization nucleation sites, consequently changing the size, number, and dispersion of the spherulite crystalline regions in the PCL matrix [66–68]. Furthermore, T_c increased due to the increase in the G and GO content (Fig. 3c), which can be attributed to the nucleating effect of the exfoliated structure of G and GO within the PCL matrix [68, 69]. However, the addition of G and GO seems to have negligible impacts on T_m (Supplementary Information). These results are consistent with previously reported findings [70–72]. Moreover, no statistical differences were

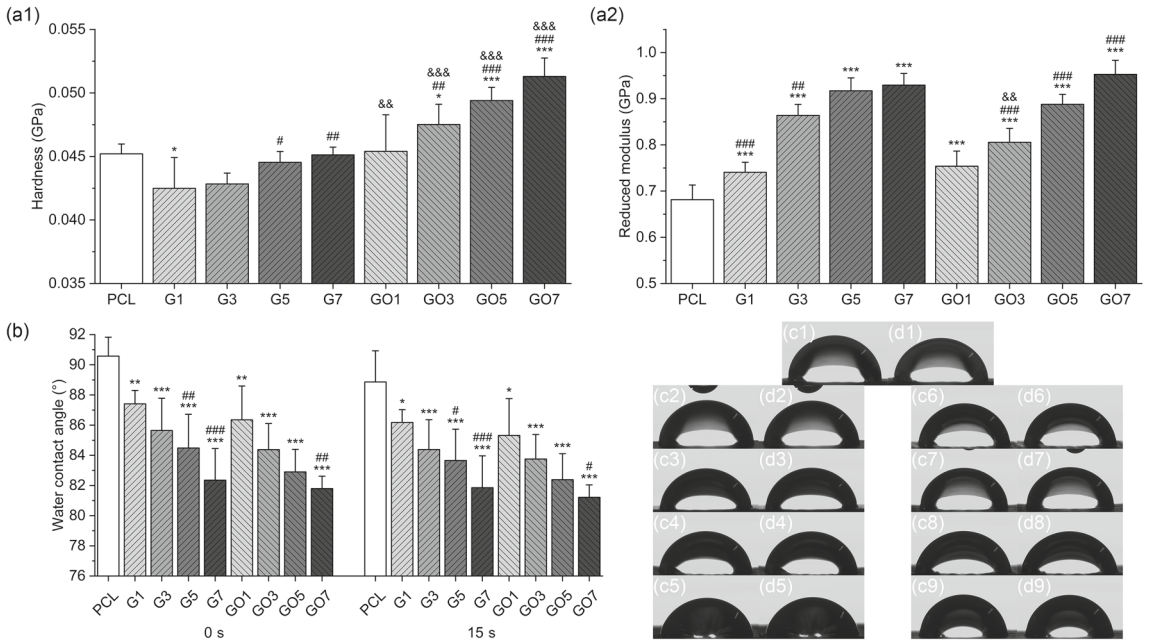

Fig. 2 **a1** Hardness and **a2** reduced modulus of polycaprolactone (PCL) and different graphene (G) and graphene oxide (GO) scaffolds. **b** Water contact angle and (**c**, **d**) droplet profiles at **c** 0 s and **d** 15 s of PCL scaffolds and different G and GO scaffolds. (**c1**, **d1**) PCL; (**c2–c5**, **d2–d5**) G1, G3, G5, and G7; (**c6–c9**, **d6–d9**) GO1, GO3, GO5, and GO7. 1, 3, 5, and 7: 1%, 3%, 5%, and 7% (mass fraction). The results were reported as mean ± standard deviation, $n = 5$. $^{*}P < 0.05$, $^{**}P < 0.01$, and $^{***}P < 0.001$: compared with PCL; $^{\#}P < 0.05$, $^{\#\#}P < 0.01$, and $^{\#\#\#}P < 0.001$: compared among the same material with different concentrations; $^{\&\&}P < 0.01$ and $^{\&\&\&}P < 0.001$: compared between different materials with the same concentration

observed on T_g, T_m, T_c, or χ_c comparing all scaffolds before and during degradation (Supplementary Information), indicating that both crystalline and amorphous regions degraded simultaneously.

Variations in mass with time

As shown in Fig. 4, the mass variation of all scaffolds exhibits a linear relation with the degradation time, according to the following equation:

$$\text{Mass}(t) = \alpha - \beta_m \times t, \tag{5}$$

where α is a constant, β_m is the mass loss rate of the scaffolds, and t is the degradation time expressed in hours.

As shown in Table 1, the incorporation of G and GO significantly increased the degradation rate, β_m, of the scaffolds, and the mass loss acceleration effect of G and GO appeared to be proportional to the filler concentrations. This effect can be attributed to several reasons. First, PCL, a biodegradable polymer, mainly undergoes hydrolytic degradation, through which ester bonds are broken by water [73]. As discussed in "Surface wettability analysis" section, the mass loss acceleration effects of G and GO can be initially attributed to the improved hydrophilicity due to the incorporation of G and GO. This is conducive to liquid intrusion into the scaffolds, which promotes the hydrolysis of ester bonds and subsequently accelerates the degradation rate [74]. Second, both G and GO are in the form of nanosheets, which can form different interfaces with the PCL matrix [75]. These interfaces function as microchannels that accelerate the degradation rate by allowing liquid intrusion into scaffolds [75]. Finally, the oxygen-containing functional groups on the surface could form hydrogen bonds, which would interact with the ester bonds, deflecting them toward the interface and making them more susceptible to be attacked by water molecules [3, 75].

Table 1 Mass loss curve fitting parameters of polycaprolactone (PCL) scaffolds and different graphene (G) and graphene oxide (GO) scaffolds

Scaffold	α	β_m	R^2
PCL	102.0293	0.1634	0.9783
G1	102.1959	0.3710	0.9864
G3	101.2945	0.9541	0.9967
G5	101.2729	1.4781	0.9871
G7	102.6528	2.0698	0.9740
GO1	102.0173	0.2705	0.9953
GO3	100.6343	0.3776	0.9982
GO5	100.0891	0.5710	0.9986
GO7	100.3936	0.7350	0.9965

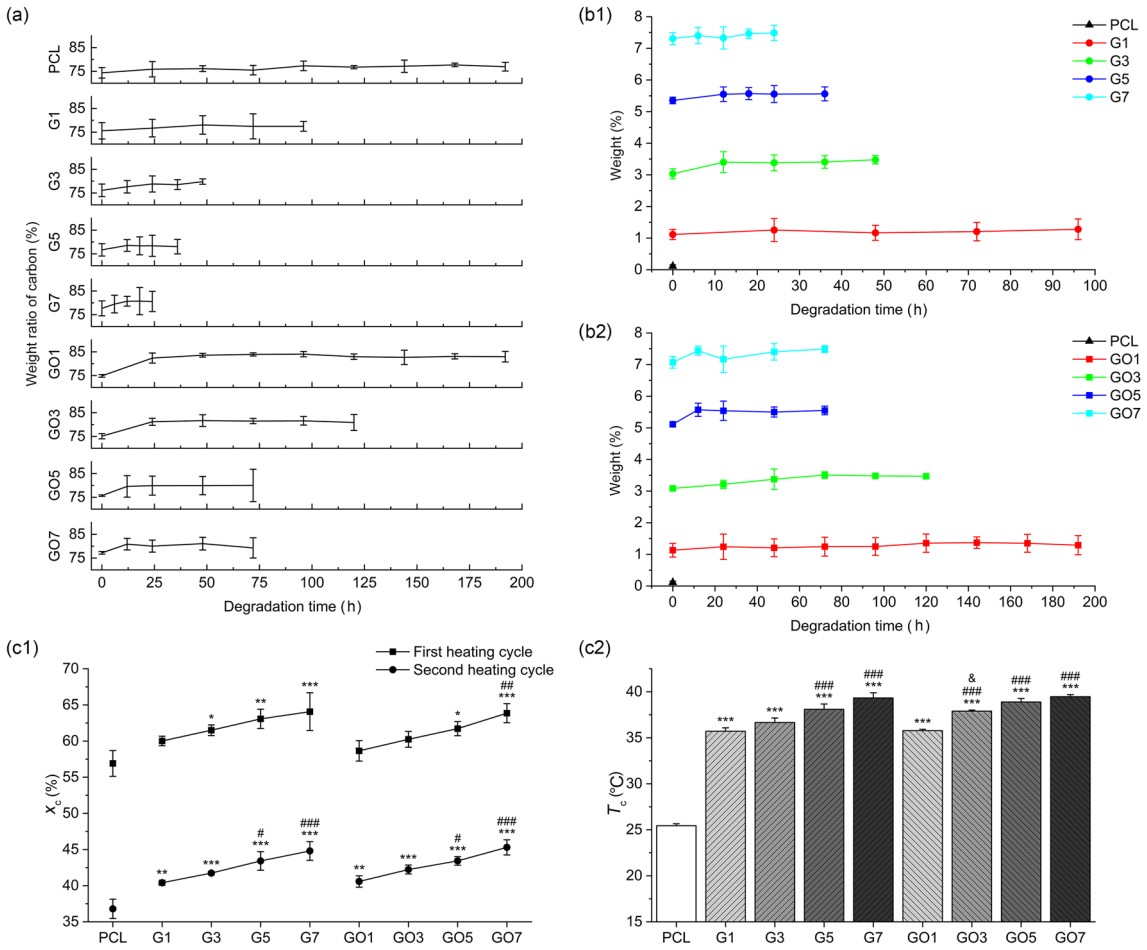

Fig. 3 **a** Element weight ratio variation with degradation time for polycaprolactone (PCL) and different graphene (G) and graphene oxide (GO) scaffolds. **b1** G and **b2** GO concentration (mass fraction) variations with degradation time for PCL and different G and GO scaffolds. **c1** Crystallinity (χ_c) and **c2** crystallization temperatures (T_c) of PCL scaffolds and different G and GO scaffolds. 1, 3, 5, and 7: 1%, 3%, 5%, and 7% (mass fraction). The results were reported as mean ± standard deviation, $n = 5$. $^{*}P < 0.05$, $^{**}P < 0.01$, and $^{***}P < 0.001$: compared with PCL; $^{\#}P < 0.05$, $^{\#\#}P < 0.01$, and $^{\#\#\#}P < 0.001$: compared among the same material with different concentrations; $^{\&}P < 0.05$: compared between different materials with the same concentration

These effects superimpose on each other and further accelerate the degradation. Several studies have reported similar results [56, 75, 76].

Variations in mechanical properties with time

The results of evaluating compressive modulus and compressive strength variation as functions of degradation time are presented in Fig. 4. As observed, printed scaffolds exhibited compressive modulus and strength similar to those of human trabecular bone (compressive modulus ranging from 50 to 1500 MPa with an average of 194 MPa, and compressive strength ranging from 1 to 30 MPa with an average of 3.55 MPa) [77–79]. The results further showed that the addition of G significantly increased compressive modulus while slightly increasing compressive strength (Fig. 5). Only G7 showed slightly lower compressive strength but without any statistical difference. In contrast, the addition of GO decreased compressive modulus and compressive strength, indicating a different trend when compared with the reduced modulus. These results can be firstly attributed to the fact that during the extrusion process, materials closer to the surface have a longer time to make contact with the screw, causing better filler alignment and homogeneous dispersion of fillers in the matrix, which ultimately leads to a strong bonding effect [80]. Secondly, particularly in the case of mechanical compression tests, by increasing the GO concentration, GO tends to stack together due to van der Waals forces, making GO more difficult to disperse, and consequently limiting load transfer [81]. These results showed that the filler is less evenly distributed in the mixture of inner material than in the material near the surface, leading to a more significant effect

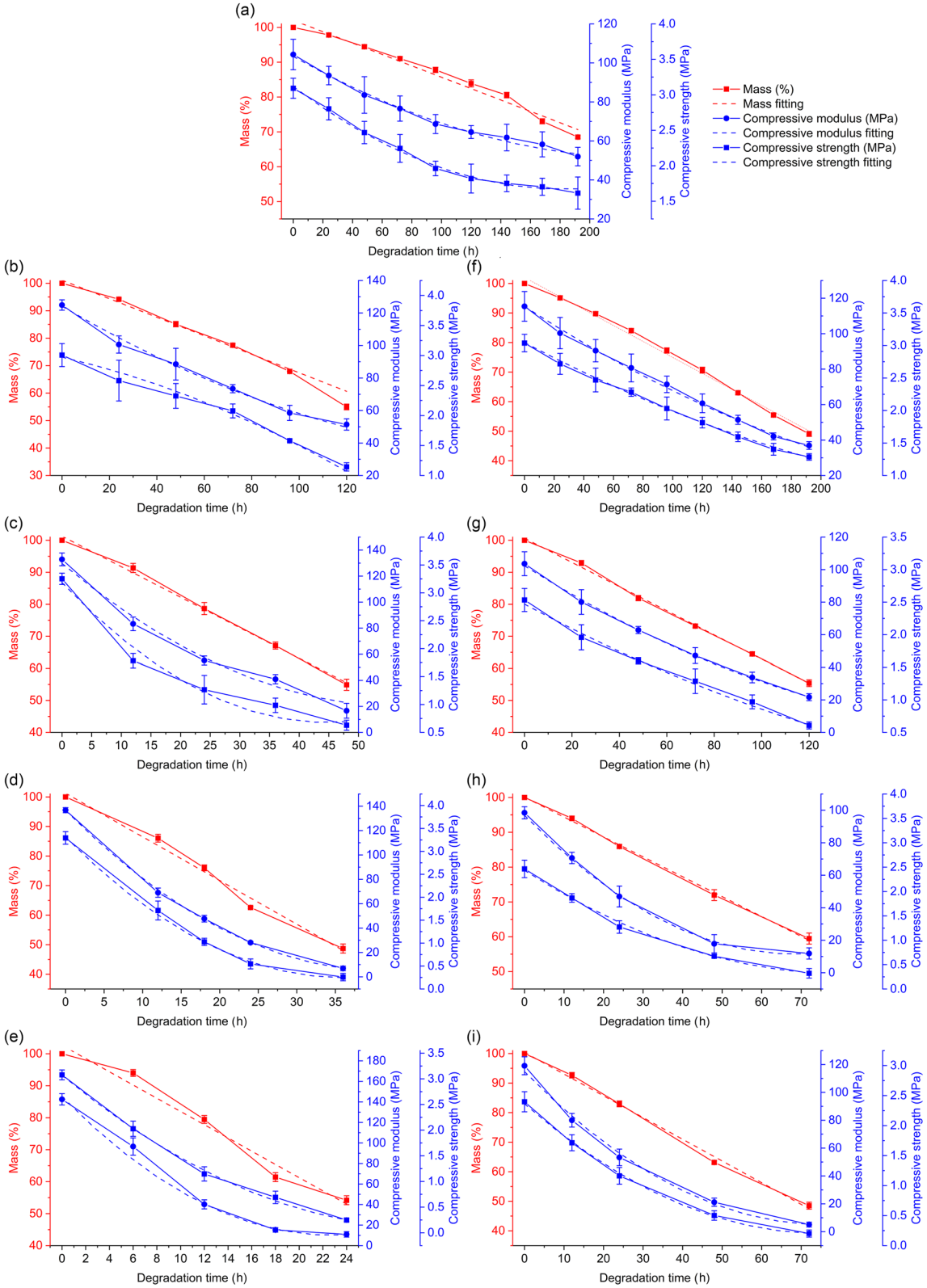

Fig. 4 Variations of mass, compressive modulus, and compressive strength as functions of degradation time for polycaprolactone (PCL) and different graphene (G) and graphene oxide (GO) scaffolds. **a** PCL; **b–e** G1, G3, G5, and G7; **f–i** GO1, GO3, GO5, and GO7. 1, 3, 5, and 7: 1%, 3%, 5%, and 7% (mass fraction). The results were reported as mean ± standard deviation, $n = 5$

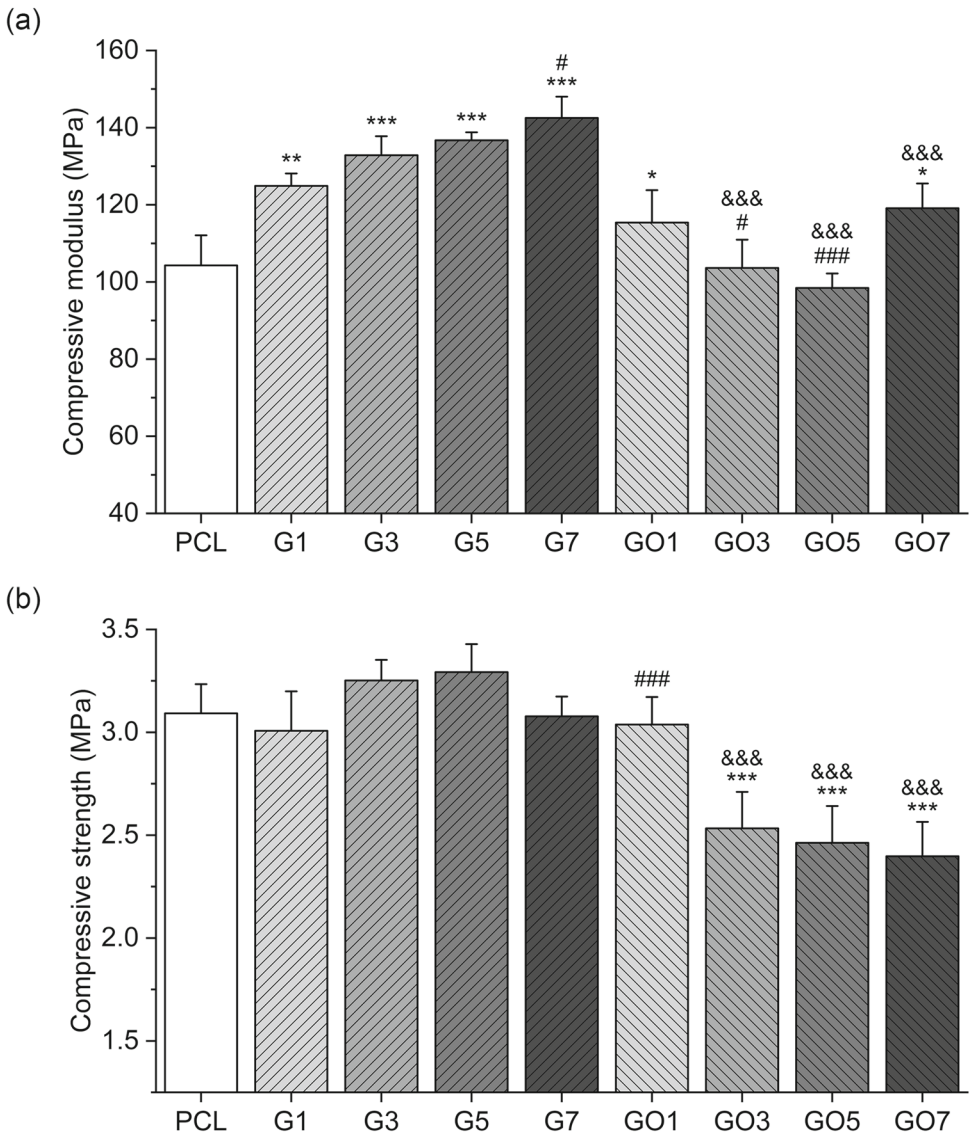

Fig. 5 **a** Compressive modulus and **b** compressive strength of polycaprolactone (PCL) and different graphene (G) and graphene oxide (GO) scaffolds. 1, 3, 5, and 7: 1%, 3%, 5%, and 7% (mass fraction). The results were reported as mean ± standard deviation, $n = 5$. $^{*}P < 0.05$, $^{**}P < 0.01$, and $^{***}P < 0.001$: compared with PCL; $^{\#}P < 0.05$ and $^{\#\#\#}P < 0.001$: compared among the same material with different concentrations; $^{\&\&\&}P < 0.001$: compared between different materials with the same concentration

of the van der Waals forces. Notably, GO7 showed a higher compressive modulus, which can be attributed to GO7 scaffolds presenting larger fiber diameters and smaller pore sizes than GO5 scaffolds.

The results also show that compressive modulus and compressive strength both decrease with the degradation time in a nonlinear manner:

$$\text{Compressive modulus}\ (t) = \text{cm}_0 - \beta_{\text{cm}} \times t + \gamma_{\text{cm}} \times t^2, \tag{6}$$

$$\text{Compressive strength}\ (t) = \text{cs}_0 - \beta_{\text{cs}} \times t + \gamma_{\text{cs}} \times t^2, \tag{7}$$

where cm_0 and cs_0 correspond to the compressive modulus and compressive strength before degradation, respectively; β_{cm} and γ_{cm} are the change coefficients of compressive modulus; β_{cs} and γ_{cs} are the change coefficients of compressive strength; and t is the degradation time expressed in hours. The curve fitting parameters in Table 2 show that the coefficients β_{cm}, γ_{cm}, β_{cs}, and γ_{cs} proportionally increase by increasing G and GO concentrations.

Variations in morphological parameters with time

Figure 6 shows SEM images of the top surface and cross-section of the scaffolds, and the zoomed-up fiber surface in the middle. Prior to degradation, the printed scaffolds present geometries close to the designed values (fiber diameter of 330 μm, top view pore size of 350 μm, and side view pore size of 210 μm), indicating that the extrusion-based additive manufacturing allows the fabrication of designed scaffolds in a reproducible way while considering optimized processing parameters. The minor variations can be attributed to the rheological properties (viscosity, viscoelastic properties,

Table 2 Compressive modulus and compressive strength curve fitting parameters of polycaprolactone (PCL) and different graphene (G) and graphene oxide (GO) scaffolds

Scaffold	Compressive modulus				Compressive strength			
	cm_0	β_{cm}	γ_{cm}	R^2	cs_0	β_{cs}	γ_{cs}	R^2
PCL	103.3012	0.4313	0.0009	0.9939	3.1160	0.0158	4.32E−5	0.9961
G1	124.2670	0.8823	0.0023	0.9971	2.9967	0.0115	− 3.32E−5	0.9947
G3	129.7487	3.8102	0.0330	0.9832	3.1824	0.1119	0.0013	0.9831
G5	136.5509	6.3605	0.0767	0.9998	3.3104	0.1697	0.0024	0.9989
G7	145.2411	11.8361	0.2590	0.9951	3.0712	0.1920	0.0031	0.9994
GO1	115.3854	0.5431	0.0007	0.9964	3.0443	0.0120	1.45E−5	0.9982
GO3	102.3466	0.9194	0.0021	0.9996	2.4691	0.0196	3.46E−5	0.9973
GO5	96.8076	2.4897	0.0182	0.9994	2.4341	0.0521	0.0003	0.9978
GO7	114.8881	2.8996	0.0191	0.9975	2.3626	0.0574	0.0004	0.9992

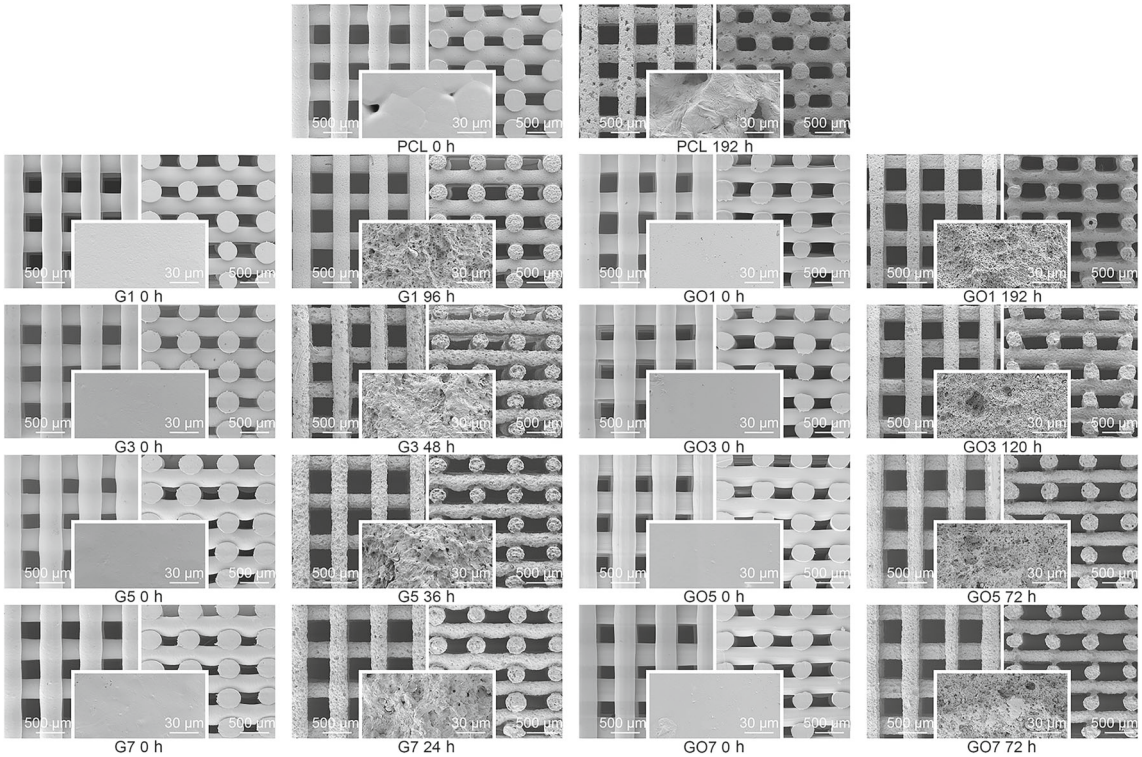

Fig. 6 Scanning electron microscopy (SEM) images of polycaprolactone (PCL) and different graphene (G) and graphene oxide (GO) scaffolds at the beginning of degradation (0 h) and before the loss of structural integrity (different time points corresponding to different scaffolds). For each time point, the left, right, and middle images represent the top surface, cross-section, and zoomed-up fiber surface, respectively

and shear-thinning) associated with different filler concentrations.

Figure 7 presents the changes in the average fiber diameter and pore size during degradation. As observed, for all scaffolds, both fiber diameter and pore size exhibit linear relationships with the degradation time:

$$\text{Fiber diameter}\ (t) = f_0 - \beta_f \times t, \tag{8}$$

$$\text{Top pore size}\ (t) = tp_0 + \beta_{tp} \times t, \tag{9}$$

$$\text{Side pore size}\ (t) = sp_0 + \beta_{sp} \times t, \tag{10}$$

where f_0 is the filament diameter before degradation; tp_0 is the top pore size before degradation; sp_0 is the side pore size before degradation; β_f, β_{tp}, and β_{sp} are the change coefficients of fiber diameter, and top and side pore sizes,

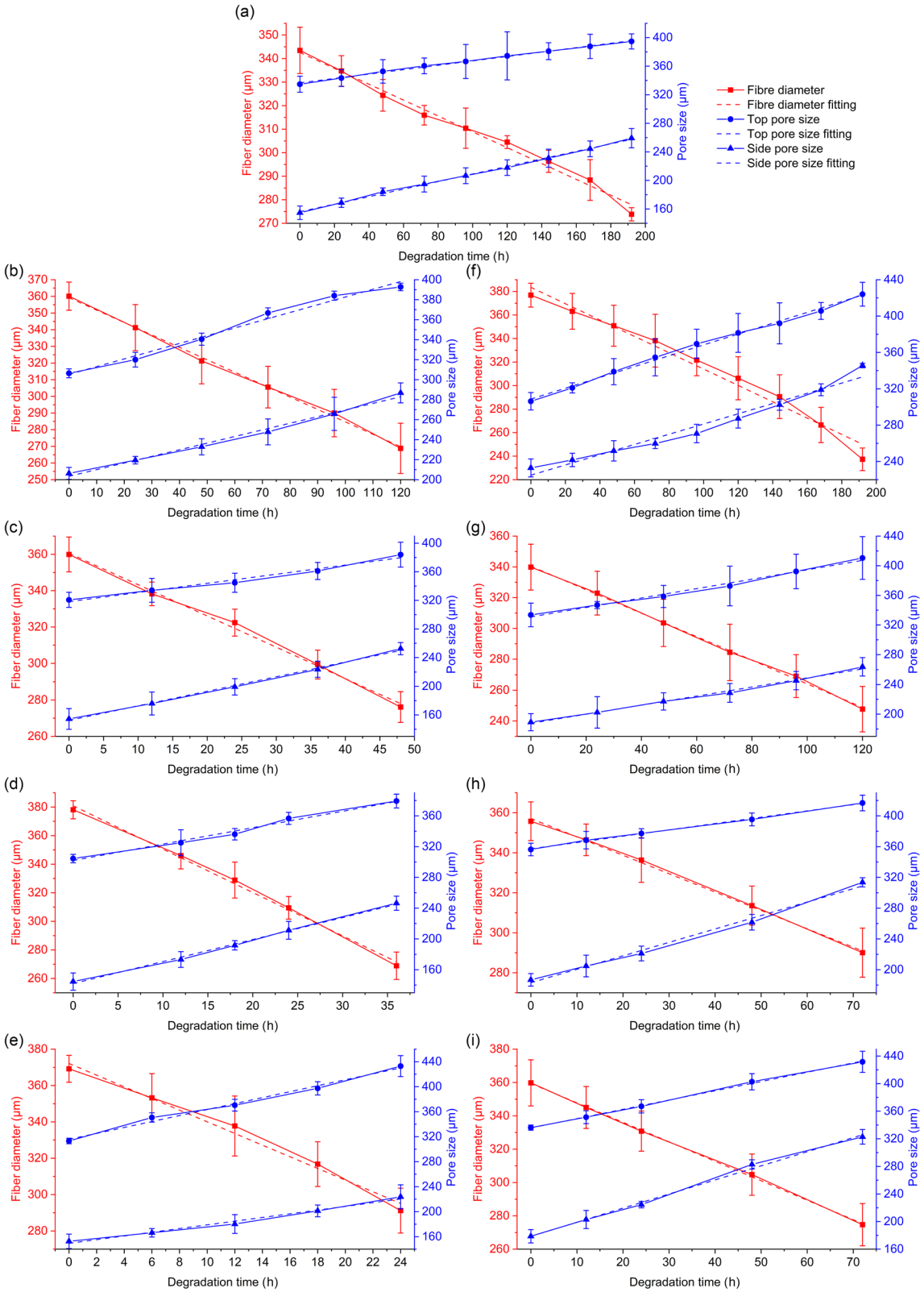

Fig. 7 Variations of both fiber diameter and pore sizes (top view and side view) as functions of degradation time for polycaprolactone (PCL) and different graphene (G) and graphene oxide (GO) scaffolds. **a** PCL; **b–e** G1, G3, G5, and G7; **f–i** GO1, GO3, GO5, and GO7. 1, 3, 5, and 7: 1%, 3%, 5%, and 7% (mass fraction). The results were reported as mean ± standard deviation, $n = 5$

Table 3 Fiber diameter and pore size curve fitting parameters of polycaprolactone (PCL) and different graphene (G) and graphene oxide (GO) scaffolds

Scaffold	Fiber diameter			Top pore size			Side pore size		
	f_0	β_f	R^2	tp_0	β_{tp}	R^2	sp_0	β_{sp}	R^2
PCL	342.5682	0.3369	0.9890	336.5913	0.3078	0.9968	156.1341	0.5285	0.9983
G1	359.2048	0.7452	0.9979	305.3062	0.7739	0.9835	203.4594	0.6624	0.9908
G3	360.4829	1.7191	0.9960	318.1934	1.2811	0.9779	152.3966	2.0332	0.9971
G5	380.8883	3.0349	0.9960	301.9042	2.1334	0.9870	141.9017	2.8615	0.9963
G7	372.1201	3.2075	0.9875	315.6349	4.7693	0.9905	149.3066	2.9584	0.9856
GO1	383.5115	0.6947	0.9791	308.6998	0.5959	0.9957	224.9536	0.5630	0.9670
GO3	340.4034	0.7633	0.9988	330.8974	0.6362	0.9896	187.6838	0.6114	0.9948
GO5	357.1174	0.9192	0.9983	357.1272	0.8212	0.9981	183.0559	1.7477	0.9922
GO7	359.4570	1.1684	0.9994	335.8283	1.3459	0.9986	178.5676	2.0459	0.9960

respectively; and t is the degradation time expressed in hours. The fitted linear relationships indicated that the scaffolds homogeneously degraded in terms of both fiber diameter and pore size. Furthermore, as shown in Table 3, the addition of G and GO increased the change coefficients β_f, β_{tp}, and β_{sp}, which also increased proportionally with G and GO concentrations.

In vitro biological characterization

Figure 8a shows the cell attachment and distribution on the scaffolds after 7 d of cell seeding, whereas Fig. 8b presents the fluorescence intensity (proportional to the amount of metabolically active cells), showing the cell proliferation on scaffolds. In all cases, the cell metabolic activity increased with time, indicating that all scaffolds were able to support the proliferation of hADSCs. At each time point, the cell viability became inversely proportional to the filler concentration. Moreover, both G1 and GO1 showed statistically higher cell viability than PCL, especially on Day 7, suggesting that the incorporation of relatively small amounts of G and GO promotes cell proliferation. This could be associated with the impacts of G and GO on the surface hardness, wettability, and roughness of the scaffolds. The increased surface stiffness promotes cellular responses, affecting cell–surface interactions [82–85]. The increased surface wettability improves the adsorption of serum proteins, which leads to a higher density of adhesion molecules available for cell attachment [85–87]. The increased surface roughness increases the adsorption of proteins and the release of local osteogenesis growth factors [85, 88, 89], all of which increase cell proliferation. In contrast, both G7 and GO7 showed statistically lowest cell viability throughout time, indicating the potential cytotoxicity effects of high concentrations of carbon nanomaterials. This phenomenon may be attributed to the increase in reactive oxygen species (ROS) resulting from the addition of carbon nanomaterials [90–92]. Moreover, in all cases, GO scaffolds exhibited lower cell viability than G scaffolds, suggesting higher cytotoxicity effects. This may be attributed to the fact that the interaction with GO generates more ROS than reduced GO materials (lower oxygen content) [93, 94], leading to intracellular protein inactivation (oxidation and nitration), lipid peroxidation, dysfunction of the mitochondria (permeabilization and release of cytochrome c), affecting nucleic acids, and eventually apoptosis or necrosis [95–98].

Conclusions

This research provides a comprehensive study on the effects of incorporating two different carbon nanomaterials, G and GO, into PCL scaffolds at different concentrations. A screw-assisted material-extrusion additive manufacturing was used to successfully fabricate 3D bone scaffolds with uniform morphologies using different composite materials.

The addition of G and GO increased the surface reduced modulus, surface hydrophilicity, scaffold crystallinity, crystallization temperature, and degradation rate, while decreasing the scaffolds' surface roughness. However, some differences were observed between G and GO. For instance, the addition of GO increased the surface hardness, whereas G only exhibited minor effects without statistical differences. Moreover, results showed that the maximum filler concentration required to achieve the highest compressive modulus and strength depended on the type of filler. In particular, the highest compressive modulus corresponded to G7 and GO7, whereas G5 and GO1 scaffolds exhibited the highest strength. The results also revealed that increasing the concentrations

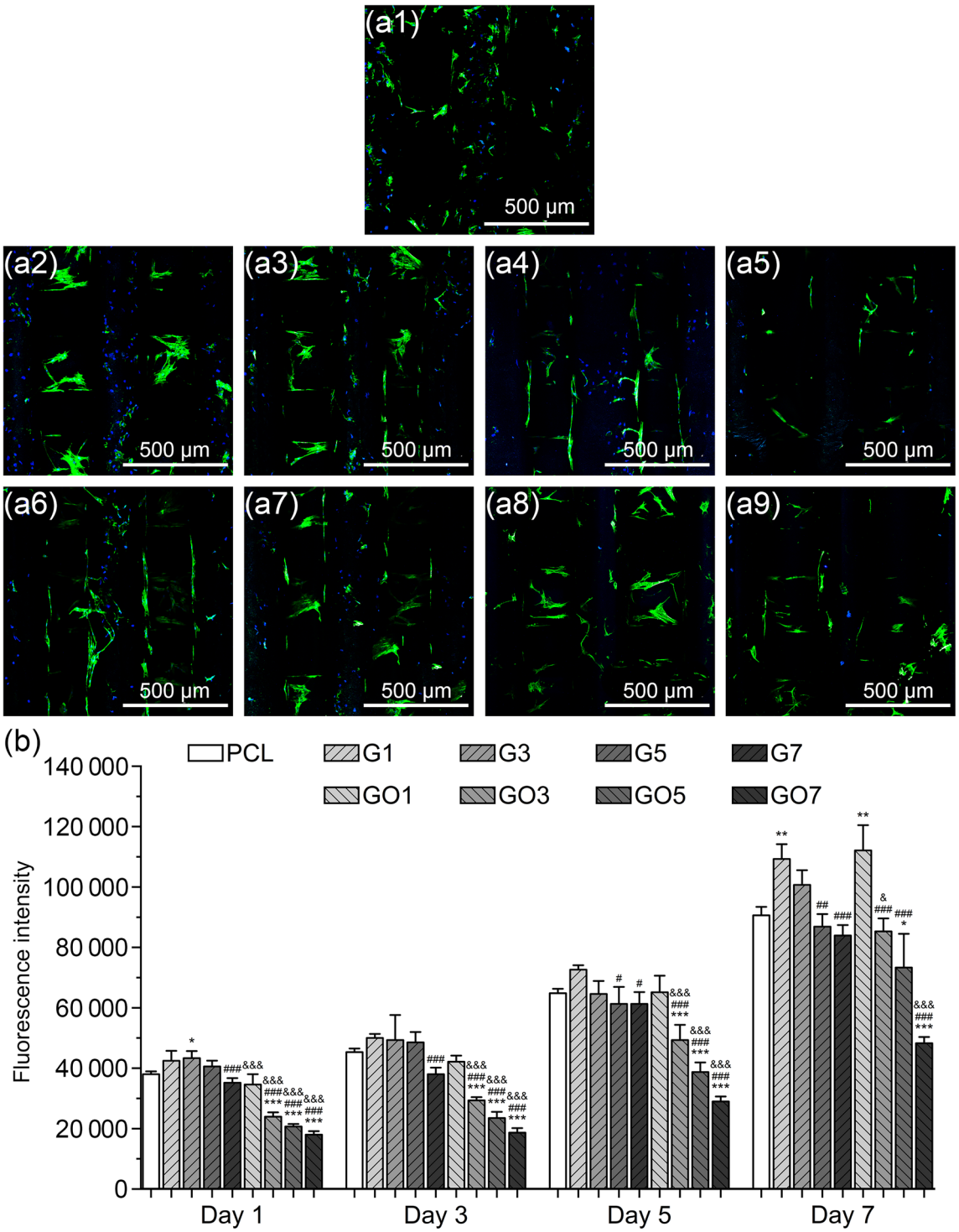

Fig. 8 **a** Confocal microscopy images of human adipose-derived stem cells (hADSCs) after 7 d of cell proliferation and **b** hADSC viability and proliferation results on polycaprolactone (PCL) and different graphene (G) and graphene oxide (GO) scaffolds. Alexa Fluor 488 (green) for F-actin and 4′,6-diamidino-2-phenylindole (DAPI) (blue) for nuclei. **a1** PCL; **a2**–**a5** G1, G3, G5, and G7; **a6**–**a9** GO1, GO3, GO5, and GO7. 1, 3, 5, and 7: 1%, 3%, 5%, and 7% (mass fraction). The results were reported as mean ± standard deviation, $n = 5$. $^{*}P < 0.05$, $^{**}P < 0.01$, and $^{***}P < 0.001$: compared with PCL; $^{\#}P < 0.05$, $^{\#\#}P < 0.01$, and $^{\#\#\#}P < 0.001$: compared among the same material with different concentrations; $^{\&}P < 0.05$ and $^{\&\&\&}P < 0.001$: compared between different materials with the same concentration

of these fillers increased surface hardness, surface reduced modulus, surface wettability, material crystallinity, crystallization temperature, and degradation rate in a proportional manner. In addition, GO exhibited higher cell toxicity than G at relatively high concentrations.

These results were correlated with the degradation time, and a range of phenomenological models describing the variations in fiber diameter, porosity, mechanical properties, and mass loss as functions of time and carbon nanomaterial concentrations were established. However, further investigation is required to understand the mechanism of how G and GO affect the biological behaviors of the scaffolds through different pathways, such as the G/GO-induced ROS and G/GO-enhanced electrical conductivity.

The findings presented in this paper, combined with previously reported results from our group [99], and the development of simulation tools, will allow us to perform computer-aided design and engineering of scaffolds to facilitate the prediction of scaffold performance after a certain period of implantation. This can be achieved by considering material parameters (functional fillers and their concentrations), topological parameters (macro- and micro-structures), and fabrication parameters (fabrication methods and processing parameters). Such an approach can help minimize the need for extensive experimental tests and improve the design of scaffolds based on their long-term performance, thus reducing the research cost and accelerating the development process.

Supplementary Information The online version contains supplementary material available at https://doi.org/10.1007/s42242-024-00280-8.

Acknowledgements The authors wish to acknowledge Engineering and Physical Sciences Research Council (EPSRC) UK for the Global Challenges Research Fund (No. EP/R015139/1), and Rosetrees Trust UK & Stoneygate Trust UK for the Enterprise Fellowship (Ref: M874).

Author contributions Conceptualization, methodology, investigation, formal analysis, validation, visualization, writing—original draft, and writing—review & editing: YHH, WGW, and PB. Supervision and funding acquisition: WGW and PB.

Declarations

Conflict of interest PB is an editorial board member for *Bio-Design and Manufacturing*, and was not involved in the editorial review or the decision to publish this article. The authors declare that there is no conflict of interest.

Ethical approval This article does not contain any studies with human or animal subjects performed by any of the authors.

References

1. Hou YH, Wang WG, Bartolo P (2022) Application of additively manufactured 3D scaffolds for bone cancer treatment: a review. Bio-Des Manuf 5(3):556–579. https://doi.org/10.1007/s42242-022-00182-7
2. Freed LE, Engelmayr GC Jr, Borenstein JT et al (2009) Advanced material strategies for tissue engineering scaffolds. Adv Mater 21(32–33):3410–3418. https://doi.org/10.1002/adma.200900303
3. Eckhart KE, Holt BD, Laurencin MG et al (2019) Covalent conjugation of bioactive peptides to graphene oxide for biomedical applications. Biomater Sci 7(9):3876–3885. https://doi.org/10.1039/c9bm00867e
4. Koski C, Bose S (2019) Effects of amylose content on the mechanical properties of starch-hydroxyapatite 3D printed bone scaffolds. Addit Manuf 30:100817. https://doi.org/10.1016/j.addma.2019.100817
5. Sarkar N, Bose S (2020) Controlled release of soy isoflavones from multifunctional 3D printed bone tissue engineering scaffolds. Acta Biomater 114:407–420. https://doi.org/10.1016/j.actbio.2020.07.006
6. Harun WSW, Kamariah MSIN, Muhamad N et al (2018) A review of powder additive manufacturing processes for metallic biomaterials. Powder Technol 327:128–151. https://doi.org/10.1016/j.powtec.2017.12.058
7. Wu H, Fahy WP, Kim S et al (2020) Recent developments in polymers/polymer nanocomposites for additive manufacturing. Prog Mater Sci 111:100638. https://doi.org/10.1016/j.pmatsci.2020.100638
8. Wang YX, Pereira RF, Peach C et al (2023) Robotic in situ bioprinting for cartilage tissue engineering. Int J Extreme Manuf 5(3):32004. https://doi.org/10.1088/2631-7990/acda67
9. Kalsi S, Singh J, Sehgal SS et al (2021) Biomaterials for tissue engineered bone scaffolds: a review. Mater Today Proc 81(2):888–893. https://doi.org/10.1016/j.matpr.2021.04.273
10. Baino F, Novajra G, Vitale-Brovarone C (2015) Bioceramics and scaffolds: a winning combination for tissue engineering. Front Bioeng Biotechnol 3:202. https://doi.org/10.3389/fbioe.2015.00202
11. Marques A, Miranda G, Silva F et al (2021) Review on current limits and potentialities of technologies for biomedical ceramic scaffolds production. J Biomed Mater Res B Appl Biomater 109(3):377–393. https://doi.org/10.1002/jbm.b.34706
12. Kulkarni SV, Nemade AC, Sonawwanay PD (2022) An overview on metallic and ceramic biomaterials. In: Dave HK, Dixit US, Nedelcu D (Eds.), Recent Advances in Manufacturing Processes and Systems. Springer Nature Singapore, Singapore, p.149–165. https://doi.org/10.1007/978-981-16-7787-8_11
13. Turnbull G, Clarke J, Picard F et al (2018) 3D bioactive composite scaffolds for bone tissue engineering. Bioact Mater 3(3):278–314. https://doi.org/10.1016/j.bioactmat.2017.10.001
14. Pugliese R, Beltrami B, Regondi S et al (2021) Polymeric biomaterials for 3D printing in medicine: an overview. Ann 3D Print Med 2:100011. https://doi.org/10.1016/j.stlm.2021.100011
15. King WE, Bowlin GL (2021) Near-field electrospinning and melt electrowriting of biomedical polymers—progress and limitations. Polymers 13(7):1097. https://doi.org/10.3390/polym13071097

16. Eivazzadeh-Keihan R, Maleki A, de la Guardia M et al (2019) Carbon based nanomaterials for tissue engineering of bone: building new bone on small black scaffolds: a review. J Adv Res 18:185–201. https://doi.org/10.1016/j.jare.2019.03.011
17. Bellet P, Gasparotto M, Pressi S et al (2021) Graphene-based scaffolds for regenerative medicine. Nanomaterials 11(2):404. https://doi.org/10.3390/nano11020404
18. Amiryaghoubi N, Fathi M, Barzegari A et al (2021) Recent advances in polymeric scaffolds containing carbon nanotube and graphene oxide for cartilage and bone regeneration. Mater Today Commun 26:102097. https://doi.org/10.1016/j.mtcomm.2021.102097
19. Feng Y, Wang ZW, Zhang RX et al (2017) Anti-fouling graphene oxide based nanocomposites membrane for oil-water emulsion separation. Water Sci Technol 77(5):1179–1185. https://doi.org/10.2166/wst.2017.634
20. Porwal H, Grasso S, Cordero-Arias L et al (2014) Processing and bioactivity of 45S5 Bioglass®-graphene nanoplatelets composites. J Mater Sci Mater Med 25(6):1403–1413. https://doi.org/10.1007/s10856-014-5172-x
21. Lopes Nalesso PR, Wang WG, Hou YH et al (2021) In vivo investigation of 3D printed polycaprolactone/graphene electro-active bone scaffolds. Bioprinting 24:e00164. https://doi.org/10.1016/j.bprint.2021.e00164
22. Huang XM, Liu LZ, Zhou S et al (2020) Physical properties and device applications of graphene oxide. Front Phys 15(3):33301. https://doi.org/10.1007/s11467-019-0937-9
23. Jiang LL, Chen DY, Wang Z et al (2019) Preparation of an electrically conductive graphene oxide/chitosan scaffold for cardiac tissue engineering. Appl Biochem Biotechnol 188(4):952–964. https://doi.org/10.1007/s12010-019-02967-6
24. Fan ZJ, Wang JQ, Liu FZ et al (2016) A new composite scaffold of bioactive glass nanoparticles/graphene: synchronous improvements of cytocompatibility and mechanical property. Colloids Surf B Biointerfaces 145:438–446. https://doi.org/10.1016/j.colsurfb.2016.05.026
25. Gao CD, Liu TT, Shuai CJ et al (2014) Enhancement mechanisms of graphene in nano-58S bioactive glass scaffold: mechanical and biological performance. Sci Rep 4(1):4712. https://doi.org/10.1038/srep04712
26. Wang WG, Huang BY, Byun JJ et al (2019) Assessment of PCL/carbon material scaffolds for bone regeneration. J Mech Behav Biomed Mater 93:52–60. https://doi.org/10.1016/j.jmbbm.2019.01.020
27. Yang YW, Peng SP, Qi FW et al (2020) Graphene-assisted barium titanate improves piezoelectric performance of biopolymer scaffold. Mater Sci Eng C 116:111195. https://doi.org/10.1016/j.msec.2020.111195
28. Ding XL, Huang Y, Li XM et al (2021) Three-dimensional silk fibroin scaffolds incorporated with graphene for bone regeneration. J Biomed Mater Res A 109(4):515–523. https://doi.org/10.1002/jbm.a.37034
29. Zhu C, He MM, Sun D et al (2021) 3D-printed multifunctional polyetheretherketone bone scaffold for multimodal treatment of osteosarcoma and osteomyelitis. ACS Appl Mater Interfaces 13(40):47327–47340. https://doi.org/10.1021/acsami.1c10898
30. Wang GY, He CX, Yang WJ et al (2020) Surface-modified graphene oxide with compatible interface enhances poly-L-lactic acid bone scaffold. J Nanomater 2020:5634096. https://doi.org/10.1155/2020/5634096
31. Shuai CJ, Zeng ZC, Yang YW et al (2020) Graphene oxide assists polyvinylidene fluoride scaffold to reconstruct electrical microenvironment of bone tissue. Mater Des 190:108564. https://doi.org/10.1016/j.matdes.2020.108564
32. Bao DS, Sun JC, Gong M et al (2021) Combination of graphene oxide and platelet-rich plasma improves tendon–bone healing in a rabbit model of supraspinatus tendon reconstruction. Regen Biomater 8(6):rbab045. https://doi.org/10.1093/rb/rbab045
33. Zhang JH, Eyisoylu H, Qin XH et al (2021) 3D bioprinting of graphene oxide-incorporated cell-laden bone mimicking scaffolds for promoting scaffold fidelity, osteogenic differentiation and mineralization. Acta Biomater 121:637–652. https://doi.org/10.1016/j.actbio.2020.12.026
34. Dinescu S, Ionita M, Ignat SR et al (2019) Graphene oxide enhances chitosan-based 3D scaffold properties for bone tissue engineering. Int J Mol Sci 20(20):5077. https://doi.org/10.3390/ijms20205077
35. Yang YW, Cheng Y, Peng SP et al (2021) Microstructure evolution and texture tailoring of reduced graphene oxide reinforced Zn scaffold. Bioact Mater 6(5):1230–1241. https://doi.org/10.1016/j.bioactmat.2020.10.017
36. Shadianlou F, Foorginejad A, Yaghoubinezhad Y (2022) Hydrothermal synthesis of zirconia-based nanocomposite powder reinforced by graphene and its application for bone scaffold with 3D printing. Adv Powder Technol 33(2):103406. https://doi.org/10.1016/j.apt.2021.103406
37. Maleki-Ghaleh H, Hossein Siadati M, Fallah A et al (2021) Effect of zinc-doped hydroxyapatite/graphene nanocomposite on the physicochemical properties and osteogenesis differentiation of 3D-printed polycaprolactone scaffolds for bone tissue engineering. Chem Eng J 426:131321. https://doi.org/10.1016/j.cej.2021.131321
38. Zhou K, Yu P, Shi XJ et al (2019) Hierarchically porous hydroxyapatite hybrid scaffold incorporated with reduced graphene oxide for rapid bone ingrowth and repair. ACS Nano 13(8):9595–9606. https://doi.org/10.1021/acsnano.9b04723
39. Bahrami S, Baheiraei N, Shahrezaee M (2021) Biomimetic reduced graphene oxide coated collagen scaffold for in situ bone regeneration. Sci Rep 11(1):16783. https://doi.org/10.1038/s41598-021-96271-1
40. Shuai C, Peng B, Liu M et al (2021) A self-assembled montmorillonite-carbon nanotube hybrid nanoreinforcement for poly-L-lactic acid bone scaffold. Mater Today Adv 11:100158. https://doi.org/10.1016/j.mtadv.2021.100158
41. Huang BY, Vyas C, Roberts I et al (2019) Fabrication and characterisation of 3D printed MWCNT composite porous scaffolds for bone regeneration. Mater Sci Eng C 98:266–278. https://doi.org/10.1016/j.msec.2018.12.100
42. Feng P, Wang K, Shuai Y et al (2022) Hydroxyapatite nanoparticles in situ grown on carbon nanotube as a reinforcement for poly (ε-caprolactone) bone scaffold. Mater Today Adv 15:100272. https://doi.org/10.1016/j.mtadv.2022.100272
43. Lemos R, Maia FR, Ribeiro VP et al (2021) Carbon nanotube-reinforced cell-derived matrix-silk fibroin hierarchical scaffolds for bone tissue engineering applications. J Mater Chem B 9(46):9561–9574. https://doi.org/10.1039/d1tb01972d
44. Hou YH, Wang WG, Bártolo P (2020) Investigating the effect of carbon nanomaterials reinforcing poly(ε-caprolactone) printed scaffolds for bone repair applications. Int J Bioprint 6(2):266. https://doi.org/10.18063/ijb.v6i2.266
45. Hou YH, Wang WG, Bártolo P (2020) Novel poly(ε-caprolactone)/graphene scaffolds for bone cancer treatment and bone regeneration. 3D Print Addit Manuf 7(5):222–229. https://doi.org/10.1089/3dp.2020.0051
46. Pitt CG, Chasalow FI, Hibionada YM et al (1981) Aliphatic polyesters. I. The degradation of poly(ϵ-caprolactone) in vivo. J Appl Polym Sci 26(11):3779–3787. https://doi.org/10.1002/app.1981.070261124
47. Sánchez-González S, Diban N, Urtiaga A (2018) Hydrolytic degradation and mechanical stability of poly(ε-caprolactone)/reduced graphene oxide membranes as scaffolds for in vitro neural tissue regeneration. Membranes 8(1):12. https://doi.org/10.3390/membranes8010012

48. ASTM International (2016) Standard test method for compressive properties of rigid cellular plastics. West Conshohocken, PA
49. ASTM International (2015) Standard test method for compressive properties of rigid plastics. West Conshohocken, PA
50. Wang MM, Wu HH, Shen CR et al (2019) Seaweed-like 2D–2D architecture of MoS_2/rGO composites for enhanced selective aerobic oxidative coupling of amines. ChemCatChem 11(7):1935–1942. https://doi.org/10.1002/cctc.201900156
51. Kuznetsov VL, Bokova-Sirosh SN, Moseenkov SI et al (2014) Raman spectra for characterization of defective CVD multi-walled carbon nanotubes. Phys Status Solidi B 251(12):2444–2450. https://doi.org/10.1002/pssb.201451195
52. Ai J, Yang L, Liao GY et al (2018) Applications of graphene oxide blended poly(vinylidene fluoride) membranes for the treatment of organic matters and its membrane fouling investigation. Appl Surf Sci 455:502–512. https://doi.org/10.1016/j.apsusc.2018.05.162
53. Kumar S, Azam D, Raj S et al (2016) 3D scaffold alters cellular response to graphene in a polymer composite for orthopedic applications. J Biomed Mater Res B Appl Biomater 104(4):732–749. https://doi.org/10.1002/jbm.b.33549
54. Seok JM, Choe G, Lee SJ et al (2021) Enhanced three-dimensional printing scaffold for osteogenesis using a mussel-inspired graphene oxide coating. Mater Des 209:109941. https://doi.org/10.1016/j.matdes.2021.109941
55. Song JQ, Gao HC, Zhu GL et al (2015) The preparation and characterization of polycaprolactone/graphene oxide biocomposite nanofiber scaffolds and their application for directing cell behaviors. Carbon 95:1039–1050. https://doi.org/10.1016/j.carbon.2015.09.011
56. Haji Mohammadi Gohari P, Haghbin Nazarpak M, Solati-Hashjin M (2021) The effect of adding reduced graphene oxide to electrospun polycaprolactone scaffolds on MG-63 cells activity. Mater Today Commun 27:102287. https://doi.org/10.1016/j.mtcomm.2021.102287
57. Weaver JK (1966) The microscopic hardness of bone. J Bone Joint Surg Am 48(2):273–288. https://doi.org/10.2106/00004623-196648020-00006
58. Luo CQ, Liao JY, Zhu ZL et al (2019) Analysis of mechanical properties and mechanical anisotropy in canine bone tissues of various ages. Biomed Res Int 2019:3503152. https://doi.org/10.1155/2019/3503152
59. Lamour G, Hamraoui A, Buvailo A et al (2010) Contact angle measurements using a simplified experimental setup. J Chem Educ 87(12):1403–1407. https://doi.org/10.1021/ed100468u
60. Dorrer C, Rühe J (2008) Drops on microstructured surfaces coated with hydrophilic polymers: Wenzel's model and beyond. Langmuir 24(5):1959–1964. https://doi.org/10.1021/la7029938
61. Khosrozadeh A, Rasuli R, Hamzeloopak H et al (2021) Wettability and sound absorption of graphene oxide doped polymer hydrogel. Sci Rep 11(1):15949. https://doi.org/10.1038/s41598-021-95641-z
62. Liu HS, Liu XY, Zhao FB et al (2020) Preparation of a hydrophilic and antibacterial dual function ultrafiltration membrane with quaternized graphene oxide as a modifier. J Colloid Interface Sci 562:182–192. https://doi.org/10.1016/j.jcis.2019.12.017
63. Al-Azzam N, Alazzam A (2022) Micropatterning of cells via adjusting surface wettability using plasma treatment and graphene oxide deposition. PLoS ONE 17(6):e0269914. https://doi.org/10.1371/journal.pone.0269914
64. Junaidi NFD, Othman NH, Fuzil NS et al (2021) Recent development of graphene oxide-based membranes for oil–water separation: a review. Sep Purif Technol 258:118000. https://doi.org/10.1016/j.seppur.2020.118000
65. Kołodziej A, Długoń E, Świętek M et al (2021) A Raman spectroscopic analysis of polymer membranes with graphene oxide and reduced graphene oxide. J Compos Sci 5(1):20. https://doi.org/10.3390/jcs5010020
66. Sayyar S, Murray E, Thompson BC et al (2013) Covalently linked biocompatible graphene/polycaprolactone composites for tissue engineering. Carbon 52:296–304. https://doi.org/10.1016/j.carbon.2012.09.031
67. Murray E, Thompson BC, Sayyar S (2015) Enzymatic degradation of graphene/polycaprolactone materials for tissue engineering. Polym Degrad Stabil 111:71–77. https://doi.org/10.1016/j.polymdegradstab.2014.10.010
68. Wang GS, Wei ZY, Sang L et al (2013) Morphology, crystallization and mechanical properties of poly(ε-caprolactone)/graphene oxide nanocomposites. Chin J Polym Sci 31(8):1148–1160. https://doi.org/10.1007/s10118-013-1278-8
69. Hua L, Kai WH, Yang JJ et al (2010) A new poly(L-lactide)-grafted graphite oxide composite: facile synthesis, electrical properties and crystallization behaviors. Polym Degrad Stabil 95(12):2619–2627. https://doi.org/10.1016/j.polymdegradstab.2010.07.023
70. Castilla-Cortázar I, Vidaurre A, Marí B et al (2019) Morphology, crystallinity, and molecular eeight of poly(ε-caprolactone)/graphene oxide hybrids. Polymers 11(7):1099. https://doi.org/10.3390/polym11071099
71. Li LY, Li CY, Ni CY (2006) Polymer crystallization-driven, periodic patterning on carbon nanotubes. J Am Chem Soc 128(5):1692–1699. https://doi.org/10.1021/ja056923h
72. Uehara H, Kato K, Kakiage M et al (2007) Single-walled carbon nanotube nucleated solution-crystallization of polyethylene. J Phys Chem C 111(51):18950–18957. https://doi.org/10.1021/jp074005v
73. Rai R, Tallawi M, Frati C et al (2015) Bioactive electrospun fibers of poly(glycerol sebacate) and poly(ε-caprolactone) for cardiac patch application. Adv Healthc Mater 4(13):2012–2025. https://doi.org/10.1002/adhm.201500154
74. Fakhrali A, Nasari M, Poursharifi N et al (2021) Biocompatible graphene-embedded PCL/PGS-based nanofibrous scaffolds: a potential application for cardiac tissue regeneration. J Appl Polym Sci 138(40):51177. https://doi.org/10.1002/app.51177
75. Shuai CJ, Li Y, Yang WJ et al (2020) Graphene oxide induces ester bonds hydrolysis of poly-L-lactic acid scaffold to accelerate degradation. Int J Bioprint 6(1):249. https://doi.org/10.18063/ijb.v6i1.249
76. Talebi A, Labbaf S, Atari M et al (2021) Polymeric nanocomposite structures based on functionalized graphene with tunable properties for nervous tissue replacement. ACS Biomater Sci Eng 7(9):4591–4601. https://doi.org/10.1021/acsbiomaterials.1c00744
77. Thomson RC, Yaszemski MJ, Powers JM et al (1996) Fabrication of biodegradable polymer scaffolds to engineer trabecular bone. J Biomater Sci Polym Ed 7(1):23–38. https://doi.org/10.1163/156856295X00805
78. Williams JM, Adewunmi A, Schek RM et al (2005) Bone tissue engineering using polycaprolactone scaffolds fabricated via selective laser sintering. Biomaterials 26(23):4817–4827. https://doi.org/10.1016/j.biomaterials.2004.11.057
79. Lotz JC, Gerhart TN, Hayes WC (1990) Mechanical properties of trabecular bone from the proximal femur: a quantitative CT study. J Comput Assist Tomogr 14(1):107–114. https://doi.org/10.1097/00004728-199001000-00020
80. Phiri J, Johansson LS, Gane P et al (2018) A comparative study of mechanical, thermal and electrical properties of graphene-, graphene oxide- and reduced graphene oxide-doped microfibrillated cellulose nanocomposites. Compos B Eng 147:104–113. https://doi.org/10.1016/j.compositesb.2018.04.018
81. Ramazani S, Karimi M (2015) Aligned poly(ε-caprolactone)/graphene oxide and reduced graphene oxide nanocomposite nanofibers: morphological, mechanical and structural properties. Mater Sci Eng C Mater Biol Appl 56:325–334. https://doi.org/10.1016/j.msec.2015.06.045

82. Engler AJ, Sen S, Sweeney HL et al (2006) Matrix elasticity directs stem cell lineage specification. Cell 126(4):677–689. https://doi.org/10.1016/j.cell.2006.06.044
83. Blacklock J, Vetter A, Lankenau A et al (2010) Tuning the mechanical properties of bioreducible multilayer films for improved cell adhesion and transfection activity. Biomaterials 31(27):7167–7174. https://doi.org/10.1016/j.biomaterials.2010.06.002
84. Discher DE, Janmey P, Wang YL (2005) Tissue cells feel and respond to the stiffness of their substrate. Science 310(5751):1139–1143. https://doi.org/10.1126/science.1116995
85. Lee WC, Lim CHYX, Shi H et al (2011) Origin of enhanced stem cell growth and differentiation on graphene and graphene oxide. ACS Nano 5(9):7334–7341. https://doi.org/10.1021/nn202190c
86. Arima Y, Iwata H (2007) Effect of wettability and surface functional groups on protein adsorption and cell adhesion using well-defined mixed self-assembled monolayers. Biomaterials 28(20):3074–3082. https://doi.org/10.1016/j.biomaterials.2007.03.013
87. Ranella A, Barberoglou M, Bakogianni S et al (2010) Tuning cell adhesion by controlling the roughness and wettability of 3D micro/nano silicon structures. Acta Biomater 6(7):2711–2720. https://doi.org/10.1016/j.actbio.2010.01.016
88. Cooper LF, Zhou YS, Takebe J et al (2006) Fluoride modification effects on osteoblast behavior and bone formation at TiO_2 grit-blasted c.p. titanium endosseous implants. Biomaterials 27(6):926–936. https://doi.org/10.1016/j.biomaterials.2005.07.009
89. Rausch-fan X, Qu Z, Wieland M et al (2008) Differentiation and cytokine synthesis of human alveolar osteoblasts compared to osteoblast-like cells (MG63) in response to titanium surfaces. Dent Mater 24(1):102–110. https://doi.org/10.1016/j.dental.2007.03.001
90. Liao CZ, Li YC, Tjong SC (2018) Graphene nanomaterials: synthesis, biocompatibility, and cytotoxicity. Int J Mol Sci 19(11):3564. https://doi.org/10.3390/ijms19113564
91. Cicuéndez M, Casarrubios L, Barroca N et al (2021) Benefits in the macrophage response due to graphene oxide reduction by thermal treatment. Int J Mol Sci 22(13):6701. https://doi.org/10.3390/ijms22136701
92. Matesanz MC, Vila M, Feito MJ et al (2013) The effects of graphene oxide nanosheets localized on F-actin filaments on cell-cycle alterations. Biomaterials 34(5):1562–1569. https://doi.org/10.1016/j.biomaterials.2012.11.001
93. Francolini I, Perugini E, Silvestro I et al (2019) Graphene oxide oxygen content affects physical and biological properties of scaffolds based on chitosan/graphene oxide conjugates. Materials 12(7):1142. https://doi.org/10.3390/ma12071142
94. Wang D, Zhu L, Chen JF et al (2015) Can graphene quantum dots cause DNA damage in cells? Nanoscale 7(21):9894–9901. https://doi.org/10.1039/c5nr01734c
95. Li Y, Liu Y, Fu YJ et al (2012) The triggering of apoptosis in macrophages by pristine graphene through the MAPK and TGF-beta signaling pathways. Biomaterials 33(2):402–411. https://doi.org/10.1016/j.biomaterials.2011.09.091
96. Wu JQ, Kosten TR, Zhang XY (2013) Free radicals, antioxidant defense systems, and schizophrenia. Prog Neuro-Psychopharmacol Biol Psychiatry 46:200–206. https://doi.org/10.1016/j.pnpbp.2013.02.015
97. Wang YF, Wang JL, Hao H et al (2016) In vitro and in vivo mechanism of bone tumor inhibition by selenium-doped bone mineral nanoparticles. ACS Nano 10(11):9927–9937. https://doi.org/10.1021/acsnano.6b03835
98. Achawi S, Feneon B, Pourchez J et al (2021) Assessing biological oxidative damage induced by graphene-based materials: an asset for grouping approaches using the FRAS assay. Regul Toxicol Pharmacol 127:105067. https://doi.org/10.1016/j.yrtph.2021.105067
99. Hou YH, Wang WG, Bartolo P (2022) Investigation of polycaprolactone for bone tissue engineering scaffolds: in vitro degradation and biological studies. Mater Des 216:110582. https://doi.org/10.1016/j.matdes.2022.110582